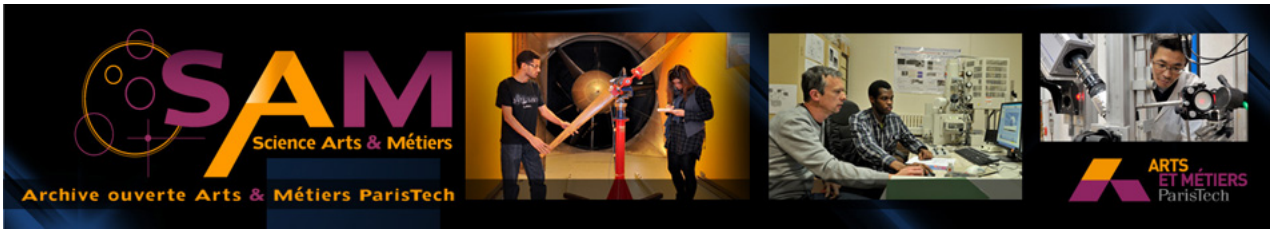

Investigation of ductility limits based on bifurcation theory coupled with continuum damage mechanics

Yasser Bouktir, Hocine Chalal, Moussa Haddad, Farid Abed-Meraim

PII: S0264-1275(15)30794-2
DOI: doi: 10.1016/j.matdes.2015.11.052
Reference: JMADE 955

To appear in:

Received date: 18 August 2015
Revised date: 9 November 2015
Accepted date: 12 November 2015

Please cite this article as: Yasser Bouktir, Hocine Chalal, Moussa Haddad, Farid Abed-Meraim, Investigation of ductility limits based on bifurcation theory coupled with continuum damage mechanics, (2015), doi: 10.1016/j.matdes.2015.11.052

Investigation of ductility limits based on bifurcation theory coupled with continuum damage mechanics

Yasser BOUKTIR [a,b], Hocine CHALAL [a,d], Moussa HADDAD [c], Farid ABED-MERAIM [a,d,*]

[a] *Laboratoire d'Étude des Microstructures et de Mécanique des Matériaux, LEM3, UMR CNRS 7239, Arts et Métiers ParisTech, 4 rue Augustin Fresnel, 57078 Metz Cedex 3, France*

[b] *Laboratoire Procédés de Fabrication, LPF, École Militaire Polytechnique, Bordj El Bahri, 16046, Algérie*

[c] *Laboratoire Mécanique des Structures, LMS, École Militaire Polytechnique, Bordj El Bahri, 16046, Algérie*

[d] *Laboratory of Excellence on Design of Alloy Metals for low-mAss Structures, DAMAS, Université de Lorraine, France*

Abstract

The ductility limits of an St14 steel are investigated using an elastic–plastic–damage model and bifurcation theory. An associative J2-flow theory of plasticity is coupled with damage within the framework of continuum damage mechanics. For strain localization prediction, the bifurcation analysis is adopted. Both the constitutive equations and the localization bifurcation criterion are implemented into the finite element code ABAQUS, within the framework of large strains and a fully three-dimensional formulation. The material parameters associated with the fully coupled elastic–plastic–damage model are calibrated based on experimental tensile tests together with an inverse identification procedure. The above-described approach allows the forming limit diagrams of the studied material to be determined, which are then compared with experimental measurements.

A main conclusion of the current study is that the proposed approach is able to provide predictions that are in good agreement with experiments under the condition of accurate material parameter calibration. The latter requires a careful identification strategy based on both calibrated finite element simulations of tensile tests at large strains and appropriately selected necking measurements. The resulting approach represents a useful basis for setting up reliable ductility limit prediction tools as well as effective parameter identification strategies.

Keywords: Ductile damage; Formability; Strain localization; Bifurcation analysis; Finite element simulation; Parameter identification.

* Corresponding author. Tel.: +(33) 3.87.37.54.79; fax: +(33) 3.87.37.54.70.
E-mail address: farid.abed-meraim@ensam.eu (F. Abed-Meraim).

1. Introduction

The concept of forming limit diagram (FLD) is probably the most common tool used in the literature to characterize the formability of sheet metals. These FLDs are usually determined experimentally or numerically by measuring, respectively, predicting the limit strains corresponding to the occurrence of localized necking in sheet metals subjected to various in-plane biaxial loading paths. The first experimental procedure for the determination of FLDs was introduced by Keeler and Backofen [1]. This experimental method consists in recording the in-plane strains at the onset of strain localization, from which the critical major and minor principal strains are extracted and reported on a curve designated as FLD. Alternatively, FLDs can be predicted by performing finite element simulations for various sheet metal forming processes (Nakazima test, Marciniak test, Bulge test, etc.), coupled with theoretical or numerical plastic instability criteria (see, e.g., [2,3]). Necking, which is a widely investigated type of plastic instability, may be classified into two categories: diffuse necking and localized necking. Considère [4] was the first to propose a unidimensional diffuse necking criterion, based on the maximum force principle, which was subsequently extended to in-plane biaxial loading by Swift [5]. Within the same family of necking criteria based on the maximum force principle, Hora et al. [6] proposed a modification to Considère's criterion for the prediction of localized necking, which accounts for the strain-path deviation in the process of strain localization. Concurrently, Hill [7] developed a bifurcation approach to predict the initiation of localized necking in an initially homogenous metal sheet subjected to in-plane biaxial stretching. However, this criterion does not predict localization in the range of positive biaxial stretching of the FLD. To remedy this limitation, some contributors combined Hill's localized necking criterion with Swift's diffuse necking criterion to predict the complete FLD (see, e.g., Firat [8], Ma et al. [2]). Subsequently, Hill [9] proposed the so-called general bifurcation approach, which is based on the loss of uniqueness for the solution of the underlying boundary value problem, for the prediction of a general class of plastic instabilities. Following the works of Hill [7,9], several criteria have been proposed based on bifurcation theory (see, e.g., Rudnicki and Rice [10], Stören and Rice [11], Rice [12]), in order to predict the localization of deformation in the form of planar shear bands as well as localized necking in thin metal sheets. From a theoretical perspective, such material instability criteria have been shown to correspond to the loss of ellipticity of the associated boundary value problem. Concurrently to the above-discussed theoretical analysis, Marciniak and Kuczynski [13] proposed an alternative approach to localized necking, based on the introduction of an initial imperfection. The latter represents the procedure the most commonly adopted in the literature for the determination of

FLDs, probably due to its versatility. Indeed, this approach can be used with different types of initial imperfection (geometric or material), and it is relatively easy to couple with a large variety of constitutive models (see, e.g., [14–17]).

In addition to a material instability criterion, the prediction of limit strains requires the use of a relevant constitutive model that describes the behavior of the sheet metal. In the past few decades, various phenomenological plasticity models coupled with ductile damage have been developed in the literature. These damage descriptions may be classified into two main approaches. The first has been popularized by the pioneering work of Gurson [18], who established a micromechanics-based damage model for porous materials. Later, several improvements have been made to the original model to take into account the nucleation and coalescence of voids (see, e.g., Tvergaard and Needleman [19], Achouri et al. [20]). The second approach is known as continuum damage mechanics (CDM) (see, e.g., Kachanov [21], Lemaitre [22], Saanouni [23]), and is based on the introduction of a phenomenological damage variable, which may be scalar isotropic or tensor-valued anisotropic, representing the surface density of microdefects. In the present work, the CDM approach, and more specifically the Lemaitre isotropic damage description, is adopted and coupled with an elastic–plastic model characterized by an associative plastic flow rule and a mixed (isotropic–kinematic) hardening law. The resulting strain-rate independent model is then combined with the Rice bifurcation criterion to predict strain localization in ductile materials. This approach is implemented into the finite element software ABAQUS within the framework of large plastic strains and a fully three-dimensional formulation.

On the other hand, a realistic prediction of strain localization requires a reliable identification of the parameters driving the mechanical behavior. In this paper, the hardening and damage parameters of the fully coupled elastic–plastic–damage model are identified using an inverse identification procedure, based on least-squares minimization of the difference between the experimental and numerical load–displacement response of a standard tensile test. The experimental tensile test was performed by Aboutalebi et al. [24] for an St14 steel material. The identified parameters, thus obtained, are then used to predict the ductility limits of the studied material, using the above-described approach that combines the elastic–plastic–damage modeling and the localization bifurcation analysis.

The remainder of the paper is structured as follows. First, the elastic–plastic constitutive equations coupled with the Lemaitre isotropic damage model are presented, and their implementation into ABAQUS using an explicit time integration scheme is outlined. Then, the Rice

localization criterion, based on bifurcation theory, is briefly described. Some numerical aspects related to mesh sensitivity are analyzed later on, in order to establish a finite element model that is applicable to the simulation of a standard tensile test. Subsequently, the hardening and damage parameters associated with the fully coupled elastic–plastic–damage model are identified based on a tensile test, using an inverse identification procedure. Thereafter, the thus identified material parameters are integrated in the above-described approach, which combines the fully coupled damage model and the localization analysis, to predict the ductility limits of the studied steel material. Finally, the obtained results are compared with experimental measurements and some discussions are drawn with regard to the significant impact of material parameter identification on the predicted ductility limits.

2. Elastic–plastic model coupled with ductile damage

2.1. Constitutive equations

In this section, the adopted elastic–plastic–damage model is briefly outlined. It consists of anisotropic associative plasticity, coupled with the continuum damage mechanics approach [22]. In the latter, damage is introduced as an isotropic variable d ($0 \le d \le 1$) that describes the surface density of microcracks. Using the strain equivalence principle [22], the usual (true) stress $\boldsymbol{\sigma}$ is related to the effective stress $\tilde{\boldsymbol{\sigma}}$ (associated with the undamaged, virgin material) as follows:

$$\tilde{\boldsymbol{\sigma}} = \frac{\boldsymbol{\sigma}}{1-d}\,. \tag{1}$$

By combining the rate form of Eq. (1) with the hypo-elastic law for the effective stress, the Cauchy stress rate tensor can be expressed as

$$\dot{\boldsymbol{\sigma}} = (1-d)\mathbf{C} : (\mathbf{D} - \mathbf{D}^{\mathrm{P}}) - \frac{\dot{d}}{1-d}\boldsymbol{\sigma}\,, \tag{2}$$

where $\mathbf{C}$ is the fourth-order elasticity tensor, while $\mathbf{D}$ and $\mathbf{D}^{\mathrm{P}}$ are the strain rate tensor and plastic strain rate tensor, respectively. The associative plastic flow rule is given by the normality law

$$\mathbf{D}^{\mathrm{P}} = \dot{\lambda}\tilde{\mathbf{V}}\,, \tag{3}$$

where $\dot{\lambda}$ is the plastic multiplier, and $\tilde{\mathbf{V}} = \partial f / \partial \boldsymbol{\sigma}$ is the flow direction, normal the yield surface f.

The yield condition, which expresses the states of plastic loading / elastic unloading, can be written in the Kuhn–Tucker form

$$f = \bar{\sigma}(\tilde{\boldsymbol{\sigma}}', \mathbf{X}) - Y \le 0 \quad ; \quad \dot{\lambda} \ge 0 \quad ; \quad \dot{\lambda} f = 0\,, \tag{4}$$

where $\bar{\sigma} = \sqrt{(\tilde{\boldsymbol{\sigma}}' - \mathbf{X}) : \mathbf{M} : (\tilde{\boldsymbol{\sigma}}' - \mathbf{X})}$ is the equivalent stress, associated with the Hill'48 quadratic yield criterion [25], function of the deviatoric part of the effective stress tensor $\tilde{\boldsymbol{\sigma}}'$ and the back-stress tensor $\mathbf{X}$, the latter being introduced to describe the kinematic hardening contribution. The fourth-order tensor $\mathbf{M}$ contains the six Hill'48 material constants, which are intended to account for the material anisotropy. The isotropic hardening contribution, which characterizes the size of the yield surface, is represented by the scalar function Y.

To derive the stress–strain constitutive equation under the following rate form:

$$\dot{\boldsymbol{\sigma}} = \mathbf{C}^{\text{ep}} : \mathbf{D}, \tag{5}$$

the plastic multiplier $\dot{\lambda}$ needs first to be determined using the consistency condition $\dot{f} = 0$ (see, e.g., [26], for more details). The analytical elastic–plastic tangent modulus $\mathbf{C}^{\text{ep}}$ in Eq. (5) thus reads

$$\mathbf{C}^{\text{ep}} = (1-d)\mathbf{C} - \alpha\left(\frac{(\mathbf{C}:\mathbf{V})\otimes(\mathbf{V}:\mathbf{C})}{H_\lambda} + \frac{H_d\tilde{\boldsymbol{\sigma}}\otimes(\mathbf{V}:\mathbf{C})}{H_\lambda}\right), \tag{6}$$

in which $\alpha = 1$ for plastic loading and 0 otherwise, $\mathbf{V} = (1-d)\tilde{\mathbf{V}}$, and H_d is a scalar modulus defining the damage evolution (i.e., such that $\dot{d} = H_d\dot{\lambda}$), which will be explicitly described later. In the above equation, the scalar modulus H_λ is given by

$$H_\lambda = (1-d)\tilde{\mathbf{V}} : \mathbf{C} : \tilde{\mathbf{V}} + (1-d)\tilde{\mathbf{V}} : \mathbf{H}_{\mathbf{X}} + H_Y, \tag{7}$$

where the second-order tensor $\mathbf{H}_{\mathbf{X}}$ represents the kinematic hardening modulus (i.e. defined such that $\dot{\mathbf{X}} = \mathbf{H}_{\mathbf{X}}\dot{\lambda}$), while H_Y denotes the scalar isotropic hardening modulus (i.e. defined such that $\dot{Y} = H_Y\dot{\lambda}$). In this work, kinematic hardening is not accounted for (i.e., the corresponding modulus $\mathbf{H}_{\mathbf{X}}$ in Eq. (7) is set to zero), and isotropic hardening is described by the following Ludwig law:

$$Y = Y_0 + k\lambda^n, \tag{8}$$

where Y_0, k, and n are the hardening-related material parameters. Note that, due to the coupling with damage, the plastic multiplier λ is used in Eq. (8) instead of the classical equivalent plastic strain $\bar{\varepsilon}^p$. The latter is related to the former by the relationship $\dot{\bar{\varepsilon}}^p = \dot{\lambda}/(1-d)$, which is derived from the plastic work equivalence principle (i.e., $\bar{\sigma}\,\dot{\bar{\varepsilon}}^{\text{p}} = (\tilde{\boldsymbol{\sigma}}' - \mathbf{X}) : \mathbf{D}^{\text{P}}$).

Finally, the evolution law for damage is given by the following expression (see, e.g., [26]):

$$\dot{d} = H_d\dot{\lambda} = \begin{cases} \dfrac{1}{(1-d)^\beta}\left(\dfrac{Y_e - Y_{ei}}{S}\right)^s \dot{\lambda} & \text{if} \quad Y_e \geq Y_{ei} \\ 0 & \text{otherwise} \end{cases}, \tag{9}$$

where β, S, s, and Y_{ei} are the damage-related material parameters, and Y_e is the elastic strain energy density release, whose expression can be found with full details in reference [26].

2.2. Time integration scheme and numerical implementation

This section outlines the implementation of the constitutive equations into a finite element code. This implementation requires the time integration of all state variables at each integration point of the finite element mesh, and for each loading increment during the finite element simulation. In this work, the Runge–Kutta explicit time integration scheme is adopted to determine the updated stress state and all internal variables at the end of each loading increment. As well-known in the literature, such an explicit procedure has the advantage of easier numerical implementation, since no sub-iterations within a given loading increment are needed to determine the updated values for the unknown state variables. Also, the derivation of the consistent (algorithmic) tangent modulus is no longer required when using an explicit finite element code such as ABAQUS/Explicit. However, the loading increments must be kept sufficiently small to ensure the overall stability and accuracy of the solution (see, e.g., Li and Nemat-Nasser [27], Safaei et al. [28]).

Assuming the stress state and internal variables are known at the beginning of loading increment, the corresponding evolution equations can be written in a compact form of differential equation

$$\dot{\mathbf{z}} = \mathbf{h}_{\mathbf{z}}\left(\mathbf{z}\right), \tag{10}$$

where vector $\mathbf{z}$ comprises all of the internal variables and stress state, while vector $\mathbf{h}_{\mathbf{z}}\left(\mathbf{z}\right)$ includes all evolution laws described in Section 2.1. This convenient global differential equation allows easily incorporating different forms of hardening laws and advanced yield surfaces, as well as various types of damage evolutions. The condensed form of evolution equation (10) is then integrated over each loading increment, using the Runge–Kutta explicit time integration scheme. The resulting algorithm is ultimately implemented into the finite element code ABAQUS/Explicit, via a VUMAT user-defined material subroutine. To take the large strain framework into account, the integration of the above fully three-dimensional formulation is achieved using a co-rotational frame, which corresponds to adopting a Jaumann-type objective derivative for the rate equations.

3. Plastic instability criterion

To predict the occurrence of strain localization, the fully coupled elastic–plastic–damage model presented in Section 2.1 is combined here with the Rice material instability criterion (see Rudnicki and Rice [10], Rice [12]). This criterion for plastic flow localization is based on a bifurcation

analysis, in which the bifurcation mode is sought in the form of an infinite localization band (see Fig. 1 for illustration). According to this theoretical approach, the condition for strain localization corresponds to the loss of ellipticity for the partial differential equations governing the associated boundary value problem. This condition is reached when the so-called acoustic tensor becomes singular for a given vector $\mathbf{n}$, which corresponds to the unit normal to the localization band (Fig. 1).

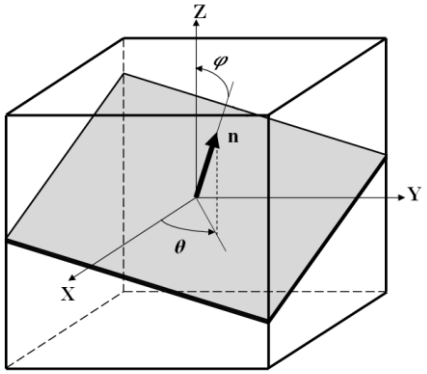

Fig. 1. Illustration of the occurrence of a localization band in an infinite block of material.

The derivation of the expression of the acoustic tensor is based on two main equations, namely, the kinematic (or compatibility) condition and the static (or equilibrium) condition. Hadamard's compatibility condition requires that the velocity field remains continuous along the discontinuity surface, which implies according to Maxwell's theorem that the discontinuity of its gradient (i.e., the jump in the velocity gradient across the localization band) must take the following form:

$$\mathbf{L} = \mathbf{L}^{+} - \mathbf{L}^{-} = \dot{\mathbf{c}} \otimes \mathbf{n}, \tag{11}$$

where $\mathbf{L}^{+}$ and $\mathbf{L}^{-}$ represent the velocity gradient outside and inside the band, respectively, while the jump amplitude $\dot{\mathbf{c}}$ characterizes the bifurcation mode (e.g., shear mode when $\dot{\mathbf{c}} \perp \mathbf{n}$).

The equilibrium condition along the localization band, which expresses the normal continuity of the nominal stress rate vector through the discontinuity surfaces, may be written as

$$\mathbf{n} \cdot \left[\!\left[\dot{\mathbf{N}} \right]\!\right] = \mathbf{n} \cdot \left(\dot{\mathbf{N}}^{+} - \dot{\mathbf{N}}^{-} \right) = \mathbf{0}, \tag{12}$$

where $\dot{\mathbf{N}}^{+}$ and $\dot{\mathbf{N}}^{-}$ represent respectively the nominal stress rate tensor outside and inside the localization band of unit normal $\mathbf{n}$. Adopting an updated Lagrangian approach, the nominal and Cauchy stress rate tensors are related to each other by the relation

$$\dot{\mathbf{N}} = \dot{\boldsymbol{\sigma}} + \boldsymbol{\sigma}\,\mathrm{tr}\left(\mathbf{D}\right) - \mathbf{L} \cdot \boldsymbol{\sigma}, \tag{13}$$

in which $\mathrm{tr}(\mathbf{D}) = \mathbf{D}:\mathbf{1}$, with $\mathbf{1}$ being the second-order identity tensor. Combining the equations above with the constitutive equations of Section 2.1, the constitutive equation is rewritten as

$$\dot{\mathbf{N}} = \mathbf{H}^{ep} : \mathbf{L}, \tag{14}$$

where the fourth-order constitutive tensor $\mathbf{H}^{ep}$ is given by the following equation:

$$\mathbf{H}^{ep} = \mathbf{C}^{ep} + \mathbf{C}_1 - \mathbf{C}_2 - \mathbf{C}_3, \tag{15}$$

where the expression of the fourth-order tangent modulus $\mathbf{C}^{ep}$ has already been given in Eq. (6), while $\mathbf{C}_1$, $\mathbf{C}_2$, and $\mathbf{C}_3$ are fourth-order tensors induced by the large strain framework. The expressions of the latter only depend on Cauchy stress components and can be found in [26,29].

Substituting the constitutive equation (14) into the equilibrium condition (12), in which the compatibility condition (11) has been exploited, yields the following linear system:

$$\mathbf{Q} \cdot \dot{\mathbf{c}} = \left(\mathbf{n} \cdot \mathbf{H}^{ep} \cdot \mathbf{n}\right) \cdot \dot{\mathbf{c}} = \mathbf{0}, \tag{16}$$

and a necessary condition for a non-trivial solution for the above eigenvalue problem provides the localization bifurcation criterion in the following form:

$$\det(\mathbf{Q}) = 0, \tag{17}$$

which is the condition of singularity of the acoustic tensor $\mathbf{Q} = \left(\mathbf{n} \cdot \mathbf{H}^{ep} \cdot \mathbf{n}\right)$, as discussed before. Note that this acoustic tensor is not symmetric, because the constitutive tensor $\mathbf{H}^{ep}$ given in Eq. (15) has none of the minor and major symmetries, due to the particular expressions of tensors $\mathbf{C}^{ep}$, $\mathbf{C}_1$, $\mathbf{C}_2$, and $\mathbf{C}_3$ (see, e.g., [26], for the full details).

4. Numerical results

4.1. Tensile test simulation

4.1.1. Finite element model

Finite element simulations of a standard tensile test are carried out in this section, using the finite element software ABAQUS/Explicit and the fully coupled elastic–plastic–damage model described in Section 2. The geometry as well as the characteristic dimensions of the specimen were taken from the work of Aboutalebi et al. [24], and are illustrated in Fig. 2. Experimental standard tensile and Vickers micro-hardness tests were performed by Aboutalebi et al. [24], on the same specimen geometry, in order to identify the material parameters. The material under study is an

St14 steel with an initial thickness of 0.8 mm. Only isotropic hardening along with a von Mises yield surface were considered in the identification procedure conducted in [24]. The corresponding identified material parameters, which will be referred to hereafter as reference parameters, are summarized in Table 1.

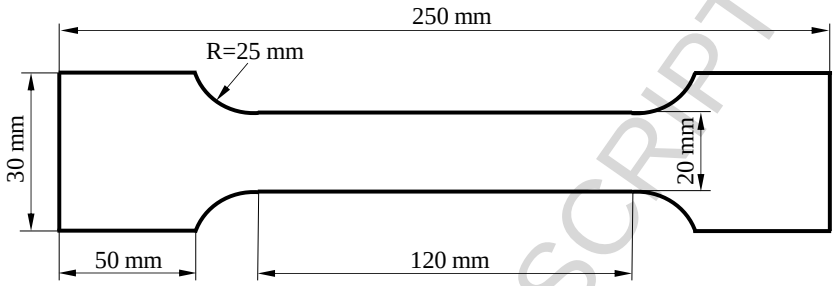

Fig. 2. Geometry and characteristic dimensions of the tensile test specimen.

Table 1

Reference material parameters for the St14 steel (from ref. [24]).

Elastic properties			
E (MPa)	ν		
$180,000$	0.33		
Ludwig hardening parameters			
Y_0 (MPa)	k (MPa)	n	
159	630	0.36	
Damage parameters			
β	S (MPa)	s	Y_{ei} (MPa)
1	2.532	1	0

4.1.2. Mesh sensitivity analysis

Due to the softening effects exhibited by the material behavior, which are induced by the evolution of damage, the associated finite element simulations are inherently prone to numerical instabilities. This well-known phenomenon, which has been widely analyzed in the literature (see, e.g., Tvergaard and Needleman [19], Peerlings et al. [30], Besson et al. [31]), leads to a strong dependence of the finite element solution on the mesh element size adopted in the simulation. In

this section, several finite element models are used in the simulation of the tensile test specimen described in Fig. 2, in order to numerically investigate the mesh sensitivity effects. In these tensile test simulations, the central region of the specimen is meshed with four different mesh sizes. The details on the mesh sizes adopted in the central region of the tensile specimen are reported in Table 2 and also illustrated in Fig. 3. For all mesh sizes, an initial element aspect ratio (width/length) is taken equal to 2 for the finite elements located in the central region of the tensile specimen (as recommended by Besson et al. [31]), which leads approximately to an element aspect ratio close to 1 at the onset of strain localization. The impact of the finite element type is also analyzed here by considering the eight-node hexahedral element with reduced integration (C3D8R) as well as the eight-node hexahedral element with incompatible modes (C3D8I), both available in the ABAQUS/Explicit software (see, e.g., the critical comparative analysis in [32]).

Table 2

Mesh sizes adopted in the simulation of the tensile test.

Mesh	length × width × thickness (mm^3)
M1	0.25 × 0.5 × 0.8
M2	0.25 × 0.5 × 0.4
M3	0.25 × 0.5 × 0.2
M4	0.33 × 0.66 × 0.2

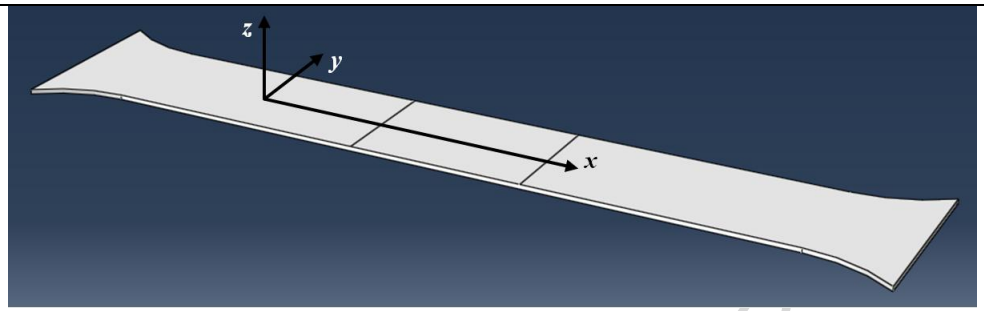

(a)

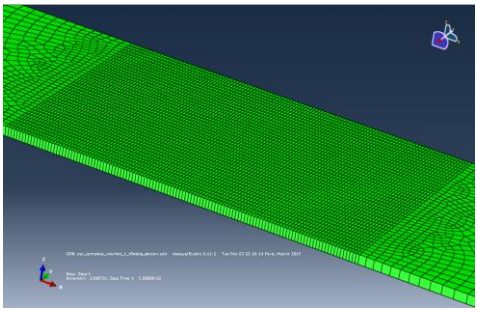

(b) Mesh size M1 = 0.25x0.5x0.8 mm^3

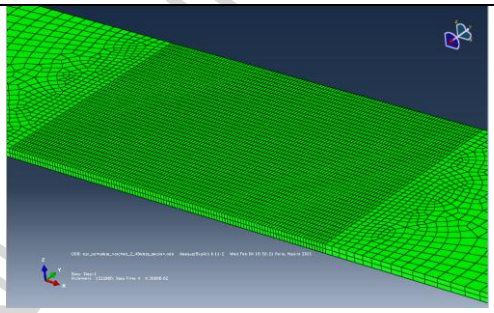

(c) Mesh size M2 = 0.25x0.5x0.4 mm^3

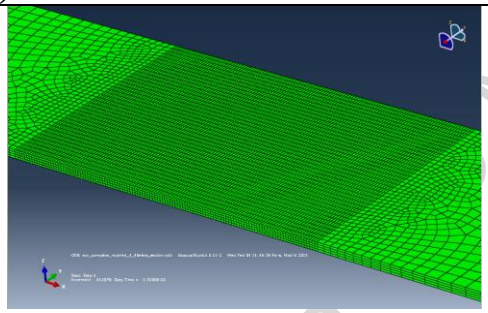

(d) Mesh size M3 = 0.25x0.5x0.2 mm^3

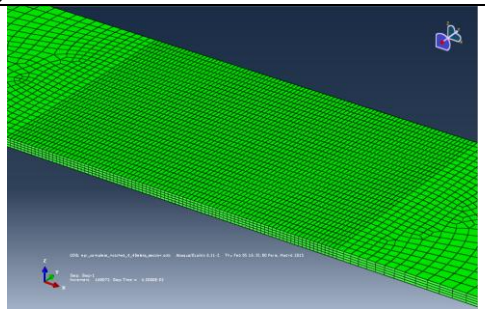

(e) Mesh size M4 = 0.33x0.66x0.2 mm^3

Fig. 3. Definition of the mesh sizes adopted in the central region of the tensile specimen.

Fig. 4 compares the simulated load–displacement responses for the tensile test obtained using the C3D8R finite element along with the different mesh sizes defined in Table 2. This figure clearly shows that the load–displacement curves are all coincident up to the onset of diffuse necking, which corresponds to the peak of the load–displacement curve. Beyond this point, and especially in the softening regime, noticeable mesh-size dependence for the solution is observed, which is characterized by an earlier drop in the load as the mesh size decreases.

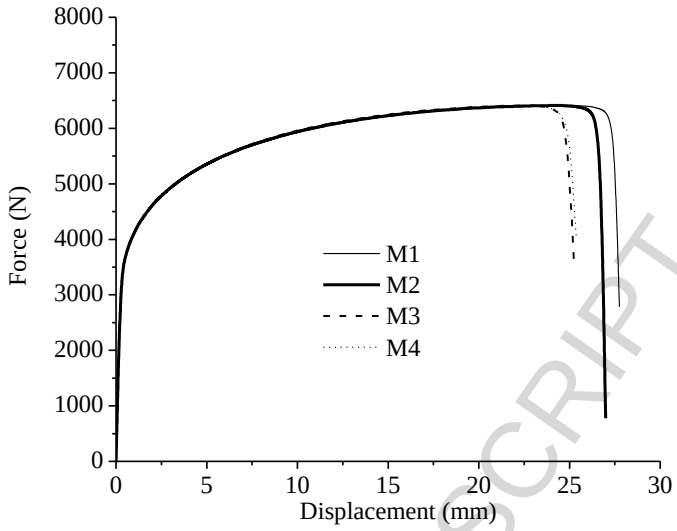

Fig. 4. Simulation of the load–displacement response for the tensile test, using the C3D8R finite element along with different mesh sizes.

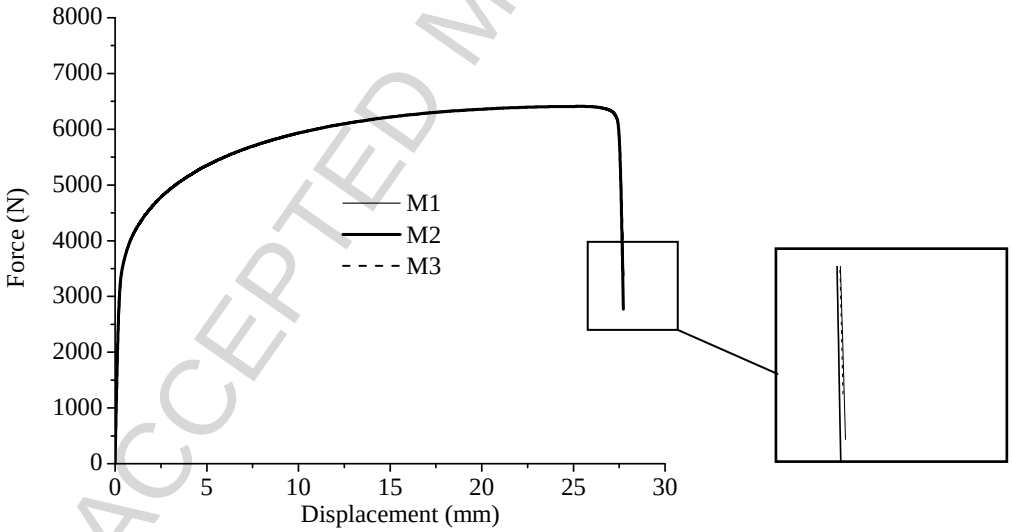

Fig. 5. Simulation of the load–displacement response for the tensile test, using the C3D8I finite element along with different mesh sizes.

Fig. 5 shows the simulated load–displacement responses for the tensile test using the C3D8I finite element along with the mesh sizes M1, M2, and M3. In contrast to the simulations obtained with the C3D8R finite element, the predicted load drop, induced by the softening behavior, does not reveal pathological mesh sensitivity when the C3D8I finite element is used. However, a very slight dependence on the mesh size is observed at final fracture, which corresponds to the complete damage of some elements located in the central region of the tensile specimen.

From the conclusions suggested by the above mesh sensitivity analysis, the C3D8I finite element with the intermediate mesh M2 will be used in the subsequent simulations of the tensile test, in order to identify the hardening and damage parameters associated with the constitutive model adopted for the St14 steel.

4.2. Identification of the material parameters

As described in Section 2, the mechanical behavior of the St14 steel material is modeled using the Ludwig isotropic hardening law, with a von Mises yield surface, coupled with the Lemaitre continuum damage approach. Tensile test experiments, as described in the previous section, were carried out by Aboutalebi et al. [24] for the studied St14 steel material. The corresponding experimental load–displacement curve is exploited in this section to identify the hardening and damage parameters for the St14 steel.

4.2.1. Ludwig hardening parameters

The hardening parameters of the Ludwig law are identified based on the range of uniform elongation in the load–displacement curve of the tensile test (i.e., up to a moderate elongation of U=15 mm). In this range of small to moderate deformations, the stress and strain fields in the central region of the specimen remain homogeneous. A simple regression of the experimental data with the Ludwig power-law defined in Eq. (8) is used to identify the hardening parameters. The corresponding identified values are reported in Table 3.

Table 3

Identified hardening parameters for the St14 steel material.

Y_0 (MPa)	k (MPa)	n
130	585	0.44

Using the identified hardening parameters above for the simulation of the tensile test, the numerical load–displacement curve is compared in Fig. 6 with that experimentally measured. It can be seen that the calibrated parameters are able to describe reasonably well the experimental hardening behavior of the St14 steel.

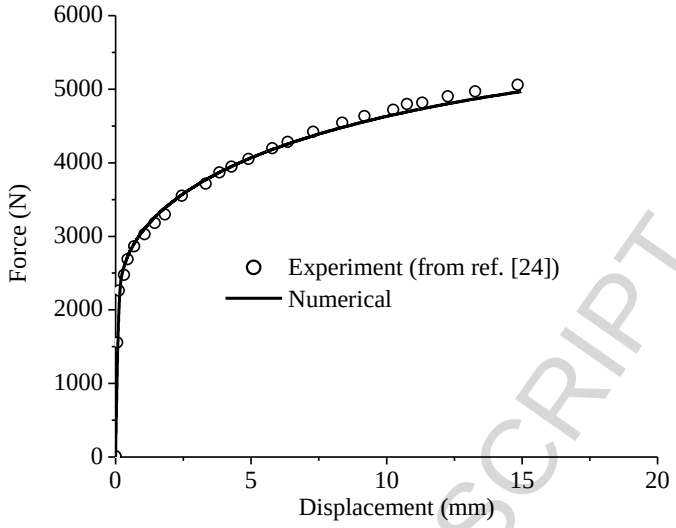

Fig. 6. Comparison between the simulated and experimental load–displacement response in the range of uniform elongation of the tensile test.

4.2.2. Damage parameter identification

The hardening parameters identified in the previous section are used here for the simulation of the tensile test until the final fracture of the specimen. The damage parameters of the Lemaitre model are identified based on the experimental load–displacement response of the tensile test using an inverse identification procedure. The latter consists in the least-squares minimization of a cost function, which represents a measure of the difference between the experimental and the finite element updated load–displacement curve of the tensile test. The identification strategy uses the *lsqnonlin* optimization function available in Matlab software, which is based on the Levenberg–Marquardt algorithm, specifically developed to solve nonlinear least-squares problems. The iterative nature of such approaches requires the use of an initial set of parameters to start the identification procedure. In this work, the damage parameters identified in ref. [24] are used in the identification algorithm as starting parameters for the identification procedure. Among the four parameters governing the damage evolution, only parameters s and Y_{ei} are identified by the present procedure, while the values of parameters β and S are kept equal to those identified in ref. [24]. The identification results for the damage parameters are summarized in Table 4.

Table 4

Identified damage parameters for the St14 steel material.

β	S	s	Y_{ei}
1	2.532	1.91	0.01

Fig. 7 compares the simulated load–displacement response, obtained using the previously identified hardening and damage parameters, with its experimental counterpart measured in ref. [24]. This comparison shows that the sudden load drop, caused by damage acceleration at the latest stages of loading, is reasonably well reproduced. This has been made possible thanks to the adopted strategy for the damage parameter identification, which exploits the entire tensile test up to large deformations.

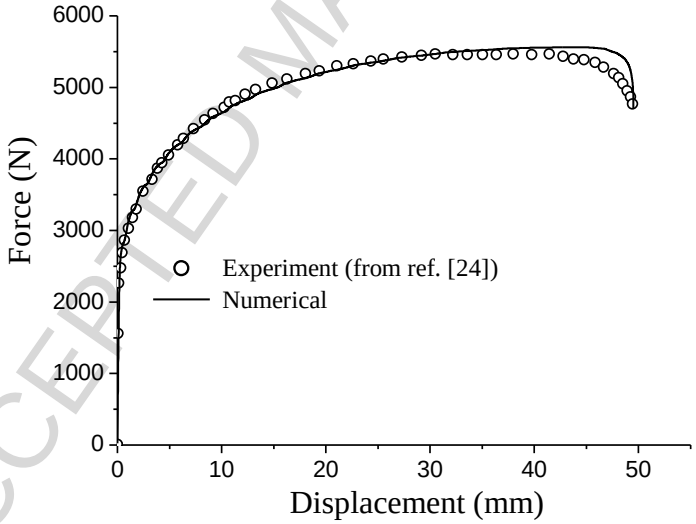

Fig. 7. Comparison between the simulated and experimental load–displacement response, up to final fracture of the tensile test.

In addition, Fig. 8 shows the distribution of the damage variable in the central area of the specimen (see Fig. 8a) at different stages of loading, determined by three-dimensional simulation of the tensile test. It can be observed that the damage distribution in the central area of the specimen remains uniform until the applied loading reaches its maximum (see Fig. 8b). Beyond this point, the damage distribution becomes heterogeneous, and concentrates increasingly in the middle of the specimen in the form of two localization bands (Fig. 8e). Finally, the accumulated damage in the narrow bands leads to highly localized necking, which ultimately results in macrocrack (Fig. 8f).

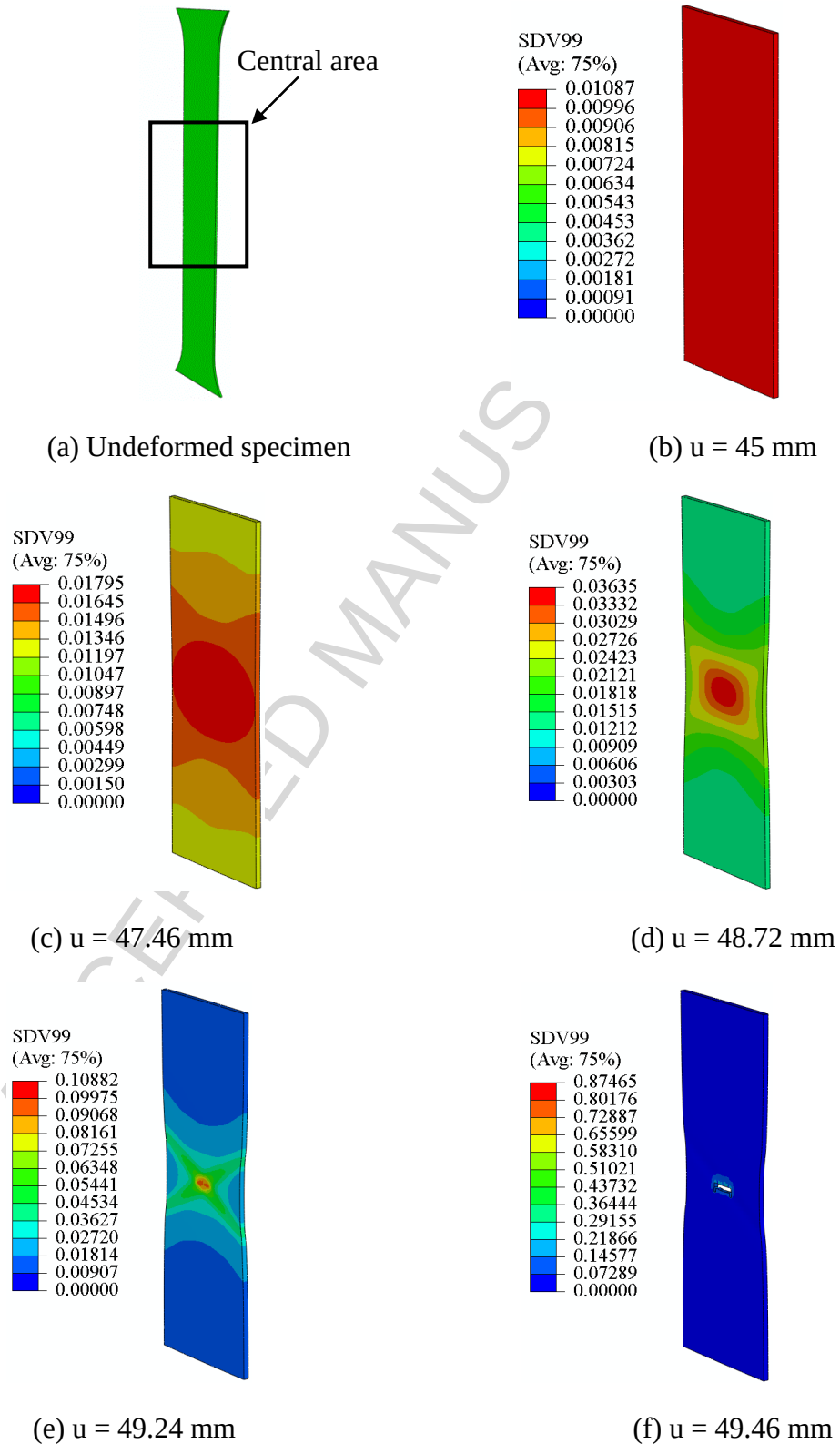

(a) Undeformed specimen (b) u = 45 mm

(c) u = 47.46 mm (d) u = 48.72 mm

(e) u = 49.24 mm (f) u = 49.46 mm

Fig. 8. Distribution of the damage variable in the central area of the specimen obtained by finite element simulation of the tensile test.

Fig. 9 shows the deformed specimen, which corresponds to a deformation state close to the final fracture, as obtained by both the numerical prediction and the experiment. As can be seen, the predicted shape of localized necking in the form of two narrow localization bands is well reproduced as compared to the experimental results.

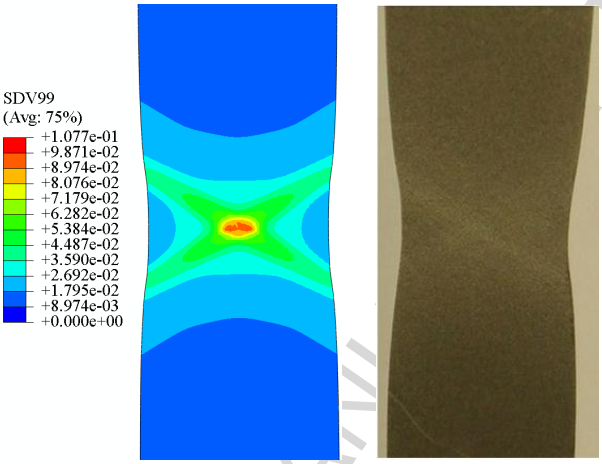

Fig. 9. Comparison between the numerical simulation of the damaged specimen and the experimental results [24] for the tensile test specimen.

4.3. Application to the FLD prediction

4.3.1. Linear in-plane strain paths

In this work, the elastic–plastic model coupled with damage is combined with localization bifurcation theory to predict FLDs for ductile materials under linear in-plane biaxial strain paths. A single finite element with one integration point (C3D8R) is considered in the simulations, in order to ensure the conditions of a homogeneous deformation state within the solid, until the occurrence of strain localization in the form of an infinite shear band. It is worth noting that, in such a boundary value problem, geometrical instabilities due to structural effects (boundary conditions, specimen geometry, etc.) are ruled out and, accordingly, only material instabilities are considered in such a bifurcation analysis.

The geometry and the boundary conditions prescribed to the single finite element model adopted for the analysis are illustrated in Fig. 10. The initial element dimensions are set equal to 1x1x1 mm^3. For the prediction of ductility limits, linear strain paths, as classically applied to biaxially stretched sheet metals, are prescribed to the single finite element. As shown in Fig. 10, the nodes (ABCD), (AEHD), and (AEFB) are clamped, respectively, along the $\vec{x}$, $\vec{y}$, and $\vec{z}$ directions, while

displacements in the $\vec{x}$ and $\vec{y}$ directions are prescribed, respectively, to the nodes (EFGH) and (FBCG). The FLD is obtained by varying the strain paths from uniaxial tension to balanced biaxial tension, thus covering the full range of strain paths that span an FLD.

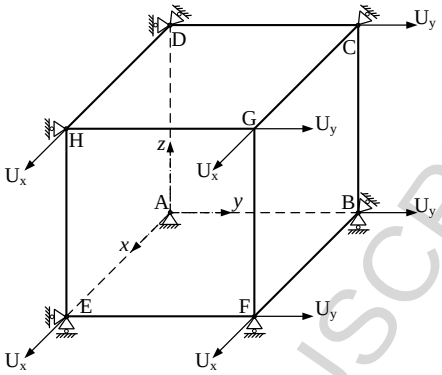

Fig. 10. Single finite element model and prescribed boundary conditions adopted for the analysis.

4.3.2. FLD prediction using the localization bifurcation analysis

In this section, the FLD of the St14 steel material is determined and compared to the experimental one, obtained from Aboutalebi et al. [33]. In order to emphasize the very significant impact of the material parameter identification on the predicted ductility limits, different values for the damage parameter β (see Eq. 9) have been considered in the simulations. In this parameter sensitivity study, only parameter β is varied, while the remaining hardening and damage parameters are kept identical to their values reported in Tables 3 and 4. The effect of varying parameter β on the load–displacement response for the tensile test is shown in Fig. 11, in which the experimental load–displacement curve is also reported for comparison. It can be observed that the load–displacement response for the tensile test is not affected by the variation of the damage parameter β in the range of uniform elongation, i.e. before the occurrence of diffuse necking, corresponding to the maximum load point (Considère [4]). From the maximum load point and up to the final fracture of the tensile specimen, the damage parameter β has only a slight influence on the load–displacement response, which makes it difficult to identify such a parameter in the post-necking range. Consequently, identifying the damage parameter β based only on a uniaxial tensile test would result in a non-negligible error on the actual value of this parameter. The impact of such potential uncertainty, regarding the proper identification of parameter β, on the prediction of FLD for the studied material is analyzed in Fig. 12. This figure shows that the damage parameter β plays a key destabilizing role in triggering plastic flow localization in the context of the adopted damage

model combined with bifurcation analysis. More specifically, increasing the value of the damage parameter β significantly lowers the predicted FLD for the studied material. This trend is consistent with the damage evolution given by Eq. (9), which clearly reveals that higher values for β tend to significantly accelerate the damage evolution, through a rapid increase in its characteristic variable d, thereby promoting early strain localization. Fig. 13 shows the evolution with deformation of the corresponding Cauchy stress and damage, until localization, along the uniaxial tensile strain path, and confirms the above discussion regarding the substantial effect of parameter β on the steep evolution of damage and its key destabilizing role in precipitating earlier flow localization. Similar trends have been consistently obtained with the other strain paths and are not reported here for conciseness.

Note that in ref. [33], the value $\beta = 1$ was originally used. With such a parameter value, the orders of magnitude revealed in Fig. 12 show that the corresponding ductility limit predictions are unrealistically high for the studied steel material (St14), as compared to the experimental results (e.g., major strain larger than 2.4 for the uniaxial tensile strain path). For higher values of β (around 12), the predicted ductility limits are in a realistic range of strains and much closer to the experimental results. As shown in Fig. 11, such high values for β have only a slight effect on the load–displacement response for the uniaxial tension test, as compared to the response obtained with $\beta = 1$. These results emphasize the difficulty of properly identifying the damage parameters using only the homogeneous range of strain allowed by the tensile test. This also suggests that by relying only on the small range of uniform deformation in the identification procedure, several values for the damage parameter β are potentially possible. Although the ductility limits are predicted at a realistic strain level for high values of β, they remain however higher than those experimentally measured (see Fig. 12). To explain this difference, one should keep in mind that the approach undertaken here, combining an elastic–plastic–damage model with the localization bifurcation approach, considers an infinite block of material subjected to a homogeneous state of stress and strain, until bifurcation into a localized band mode is detected. Structural instabilities, such as diffuse necking, and the associated geometric effects are purposely excluded in this analysis, while these are inherently unavoidable in experiments. Consequently, the critical localization strains predicted with the present approach should be viewed as limits to ductility set by material instability in the constitutive description and, as such, are expected to provide upper bounds to those determined experimentally (see, e.g., the detailed discussion in ref. [29]).

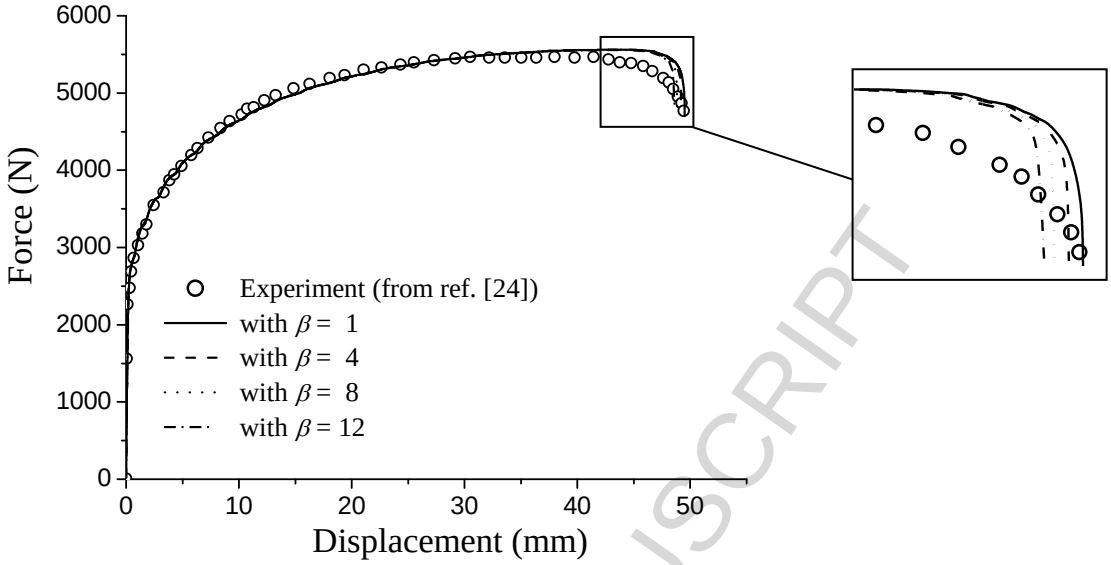

Fig. 11. Effect of the damage parameter β on the predicted load–displacement response for the uniaxial tensile test and comparison with experiment.

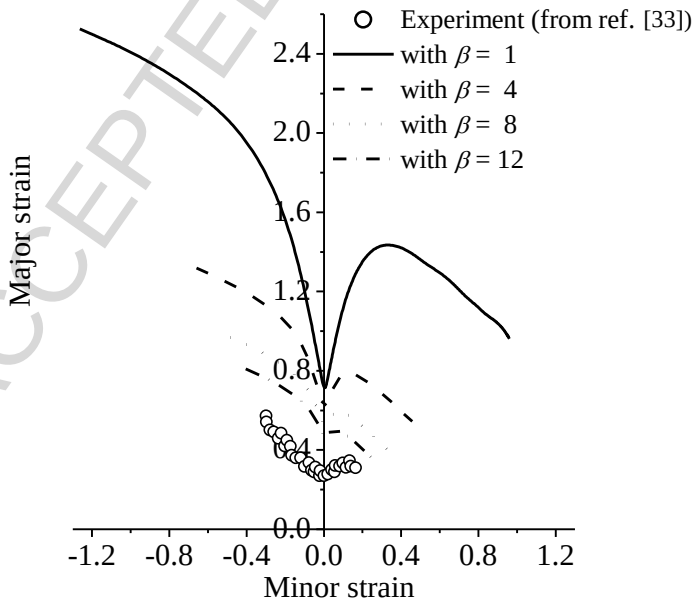

Fig. 12. Effect of variation of the damage parameter β on the predicted FLD.

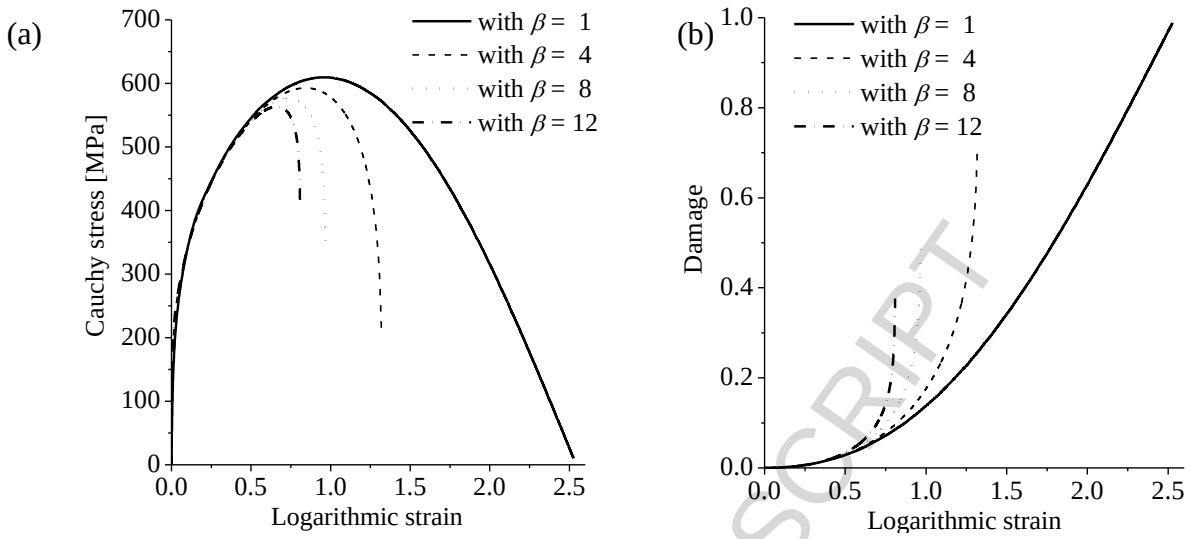

Fig. 13. True stress–strain response and damage evolution until localization for the St14 steel under uniaxial tensile strain path.

5. Conclusion

A fully anisotropic elastic–plastic model coupled with the continuum damage theory has been combined with a strain localization criterion, based on bifurcation theory, to predict the ductility limits of metallic materials. The main contributions and conclusions from this study are as follows:

- The resulting theoretical/numerical prediction tool has been formulated within a large strain fully three-dimensional framework and implemented into a finite element software package;
- The material parameters of the studied St14 steel, which are associated with both the isotropic hardening law and the continuum damage model, have been identified using an experimental load–displacement response of a standard tensile test and an inverse identification procedure;
- The identified parameters have been used to predict the FLDs of the St14 steel. A parameter sensitivity study revealed that one of the damage parameters has a very strong impact on strain localization, while its effect on the load–displacement curve is only perceptible at final fracture;
- This work emphasizes the impact of uncertainty in parameter identification on FLD prediction. An identification procedure based only on a uniaxial tensile test would result in non-negligible errors on material parameter values and, consequently, large scatter in the associated FLDs;
- The obtained results suggest integrating the proposed localization bifurcation approach, and the associated prediction tool, in the identification procedure itself, in order to improve the accuracy and reliability of the material parameters thus calibrated at large strains.

References

[1] S.P. Keeler, W.A. Backofen, Plastic instability and fracture in sheet stretched over rigid punches, ASM Transactions Quarterly 56 (1964) 25–48.

[2] X. Ma, F. Li, J. Li, Q. Wang, Z. Yuan, Y. Fang, Analysis of forming limits based on a new ductile damage criterion in St14 steel sheets, Mater. Des. 68 (2015) 134–145.

[3] F. Zhalehfar, S.J. Hosseinipour, A different approach for considering the effect of non-proportional loading path on the forming limit diagram of AA5083, Mater. Des. 50 (2013) 165–173.

[4] A. Considère, Mémoire sur l'emploi du fer et de l'acier dans les constructions, Ann. Ponts et Chaussées 9 (1885) 574–775.

[5] H.W. Swift, Plastic instability under plane stress, J. Mech. Phys. Solids 1 (1952) 1–18.

[6] P. Hora, L. Tong, J. Reissner, A prediction method of ductile sheet metal failure in FE simulation, in: Proceedings of Numisheet'96, Michigan, USA; 1996, p. 252–256.

[7] R. Hill, On discontinuous plastic states, with special reference to localized necking in thin sheets, J. Mech. Phys. Solids 1 (1952) 19–30.

[8] M. Firat, A finite element modeling and prediction of stamping formability of a dual-phase steel in cup drawing, Mater. Des. 34 (2012) 32–39.

[9] R. Hill, A general theory of uniqueness and stability in elastic–plastic solids, J. Mech. Phys. Solids 6 (1958) 236–249.

[10] J.W. Rudnicki, J.R. Rice, Conditions for the localization of deformation in pressure sensitive dilatant materials, J. Mech. Phys. Solids 23 (1975) 597–605.

[11] S. Stören, J.R. Rice, Localized necking in thin sheets, J. Mech. Phys. Solids 23 (1975) 421–441.

[12] J.R. Rice, The localization of plastic deformation, in: Theoretical and Applied Mechanics, 14th Inter. Congress on Theor. Appl. Mech., Delft, Netherlands; 1976, p. 207–220.

[13] Z. Marciniak, K. Kuczynski, Limit strains in the process of stretch forming sheet metal, Int. J. Mech. Sci. 9 (1967) 609–620.

[14] A. Ghazanfari, A. Assempour, Calibration of forming limit diagrams using a modified Marciniak–Kuczynski model and an empirical law, Mater. Des. 34 (2012) 185–191.

[15] S. Panich, F. Barlat, V. Uthaisangsuk, S. Suranuntchai, S. Jirathearanat, Experimental and theoretical formability analysis using strain and stress based forming limit diagram for advanced high strength steels, Mater. Des. 51 (2013) 756–766.

[16] X. Li, G. Guo, J. Xiao, N. Song, D. Li, Constitutive modeling and the effects of strain-rate and temperature on the formability of Ti–6Al–4V alloy sheet, Mater. Des. 55 (2014) 325–334.

[17] M. Ben Bettaieb, F. Abed-Meraim, Investigation of localized necking in substrate-supported metal layers: Comparison of bifurcation and imperfection analyses, Int. J. Plast. 65 (2015) 168–190.

[18] A.L. Gurson, Continuum theory of ductile rupture by void nucleation and growth: Part I – Yield criteria and flow rules for porous ductile media, J. Eng. Mat. Tech. 99 (1977) 2–15.

[19] V. Tvergaard, A. Needleman, Analysis of the cup-cone fracture in a round tensile bar, Acta Metall. Mater. 32 (1984) 157–169.

[20] M. Achouri, G. Germain, P. Dal Santo, D. Saidane, Experimental characterization and numerical modeling of micromechanical damage under different stress states, Mater. Des. 50 (2013) 207–222.

[21] L.M. Kachanov, Introduction to continuum damage mechanics, Springer, Netherlands, 1986.

[22] J. Lemaitre, A course on damage mechanics, Springer-Verlag, Berlin, Heidelberg, 1992.

[23] K. Saanouni, Damage Mechanics in Metal Forming: Advanced Modeling and Numerical Simulation, ISTE, John Wiley & Sons, 2012.

[24] F.H. Aboutalebi, M. Farzin, M. Poursina, Numerical simulation and experimental validation of a ductile damage model for DIN 1623 St14 steel, Int. J. Adv. Manuf. Tech. 53 (2011) 157–165.

[25] R. Hill, A theory of the yielding and plastic flow of anisotropic metals, Proc. Royal Soc. A 193 (1948) 281–297.

[26] B. Haddag, F. Abed-Meraim, T. Balan, Strain localization analysis using a large deformation anisotropic elastic–plastic model coupled with damage, Int. J. Plasticity 25 (2009) 1970–1996.

[27] Y.-F. Li, S. Nemat-Nasser, An explicit integration scheme for finite deformation plasticity in finite-element methods, Finite Elem. Anal. Des. 15 (1993) 93–102.

[28] M. Safaei, M.-G. Lee, W. De Waele, Evaluation of stress integration algorithms for elastic–plastic constitutive models based on associated and non-associated flow rules, Comput. Methods Appl. Mech. Engrg. 295 (2015) 414–445.

[29] L.Z. Mansouri, H. Chalal, F. Abed-Meraim, Ductility limit prediction using a GTN damage model coupled with localization bifurcation analysis, Mech. Mater. 76 (2014) 64–92.

[30] R.H.G. Peerlings, M.G.D. Geers, R. de Borst, W.A.M. Brekelmans, A critical comparison of nonlocal and gradient-enhanced softening continua, Int. J. Solids Struct. 38 (2001) 7723–7746.

[31] J. Besson, D. Steglich, W. Brocks, Modeling of plane strain ductile rupture, Int. J. Plasticity 19 (2003) 1517–1541.

[32] A. Salahouelhadj, F. Abed-Meraim, H. Chalal, T. Balan, Application of the continuum shell finite element SHB8PS to sheet forming simulation using an extended large strain anisotropic elastic–plastic formulation, Arch. Appl. Mech. 82 (2012) 1269–1290.

[33] F.H. Aboutalebi, M. Farzin, M. Mashayekhi, Numerical predictions and experimental validations of ductile damage evolution in sheet metal forming processes, Acta Mech. Solida Sinica 25 (2012) 638–650.

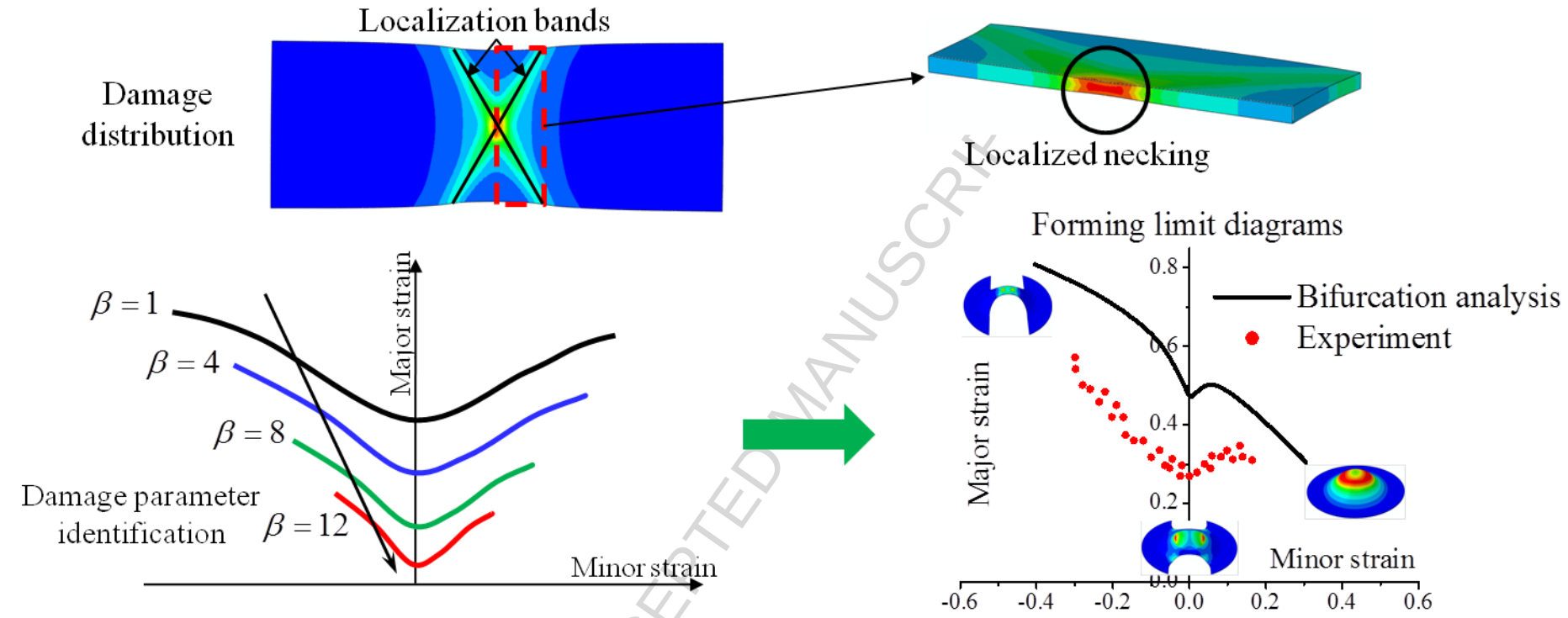

Graphical abstract

Highlights:

- An elastic–plastic–damage model is combined with localization bifurcation analysis.
- The resulting tool is applied to predict forming limit diagrams of real materials.
- Damage identification inaccuracy has significant impact on formability prediction.
- The proposed approach contributes to reliable identification of damage parameters.